RESEARCH

Open Access

CrossMark

Multistatic adaptive CFAR detection in non-Gaussian clutter

Riccardo Palamà, Maria Greco*(iD) and Fulvio Gini

Abstract

This work addresses the problem of target detection for multistatic radars. We propose an algorithm that is able to keep constant the false alarm rate, when the disturbance samples associated with each receiver-transmitter pair are distributed according to a compound Gaussian model. The performance of the proposed detection algorithm are analysed to assess the impact of clutter diversity on detection performance. The results show that clutter statistical diversity has a strong impact on detection performance. The performance of both single-channel and multichannel detection schemes are evaluated by processing real sea clutter data collected by the NetRAD nodes, in order to evaluate which of the two channels, i.e. the bistatic and monostatic channels, is more favourable for target detection. Furthermore, the gain achieved by using a multistatic detection algorithm is also analysed.

1 Introduction

Sea clutter is typically non-Gaussian and non-stationary, which makes the design of proper detection algorithms a critical task. The development of radar detection algorithms in the presence of Gaussian or non-Gaussian disturbance has been widely addressed in literature and is still an active research field. In the case of non-Gaussian disturbance, one of the most used algorithms is the so-called normalized matched filter (NMF) [1–3]. Under the hypothesis of compound Gaussian clutter, this algorithm is able to keep constant the false alarm rate (FAR). This property is verified both when the clutter covariance matrix is a priori known and when it is unknown and estimated from the range cells surrounding the range cell under test (in this case, we use the adaptive version of the NMF, i.e. the normalized adaptive matched filter (NAMF) [4–6]). The fast temporal fluctuations of the clutter make its samples to be only partially correlated in short times and broaden the clutter spectrum. The correlation properties are described, from a statistical standpoint, by the clutter covariance matrix.

The use of multiple transmitters and receivers in a radar system aims at improving the target detection, tracking and recognition capabilities of a radar system [7–13]. Radar detection techniques for multistatic radars

can be distinguished between centralized and decentralized ones. According to a centralized detection scheme, the signals associated with each transmitter-receiver pair are processed locally at each receiver node, which computes a local statistic, and then, all the local statistics are transmitted to a central processor, which in turn computes a global statistic [7, 9]. The hard decision is performed by comparing this global statistic with a threshold. An alternative detection rule is the decentralized one (see, e.g. [14–17]), according to which each node performs a hard decision, then transmits the resulting binary symbols to a central processor, that executes the final decision. One of the main limitations of a centralized detection technique is that it requires a large bandwidth of the communication link between the system nodes. If the communication bandwidth is not sufficiently large, the local statistics, transmitted by each node to the central processor, may be distorted [18]. For this reason, in real systems, the local statistics are quantized and then transmitted to the central processor; thus, a quantization noise is present. In this work, a centralized detection rule is considered, without accounting for the limitations associated with a communication link with finite bandwidth, as the aim of the work is to study the effect of clutter diversity on the detection performance of a multistatic radar system.

One of the first works dealing with the design of centralized detection for multistatic radar is Conte et al.'s paper [7] that proposes both optimum and suboptimum

* Correspondence: m.greco@iet.unipi.it
Dipartimento di Ingegneria dell'Informazione, University of Pisa, Via G. Caruso 16, Pisa, Italy

detection algorithms in the case of white Gaussian noise. In [8], the authors discuss again the optimum and suboptimum multistatic radar detection techniques in the cases that clutter and jamming are Gaussian and correlated with both time and space. A multichannel detection technique, under cross-correlated Gaussian channels, is proposed in [19], where a multichannel generalized likelihood ratio test (GLRT) is derived. More recently, the interest of the radar community towards Multi-Input Multi-Output (MIMO) radar systems has encouraged the research on multichannel detection techniques. MIMO radars can be distinguished, based on the location of their nodes, between collocated and not collocated (also known as widely separated MIMO). In a collocated MIMO radar [11], the transmitter and receiver antennas are in the same location; thus, the diversity is achieved by using antennas with a certain number of elements, each of them transmitting a different waveform. Hence, the diversity gain is guaranteed by the fact that each element of the receiver antenna looks at a different channel. In the case of widely separated radars, transmitter and receiver locations are not the same; thus, the signals associated with each transmitter-receiver pair—if combined together in a correct way—can provide a diversity gain, due to the spatial separation between channels [10, 13]. The optimum detection technique for MIMO radars in the cases of Gaussian and spatially uncorrelated clutter, called MIMO-Optimum Gaussian Detector (MIMO-OGD), has been discussed in [13]. In [20], the authors evaluate the performance of the MIMO-OGD, compared with a decentralized detection scheme. A detection algorithm for MIMO radar that utilizes space-time coded waveforms is derived and discussed in [12]. A MIMO-GLRT, based on a parametric approach, is proposed and validated in [21]. In [22], a MIMO-GLRT and Rao detector are derived in the case of non-Gaussian clutter, and their performance are evaluated in the case of known covariance matrix.

In this work, we consider a multichannel extension of the NMF, introduced with the name of MIMO-Generalized Likelihood Ratio Test-Linear Quadratic (MIMO-GLRT-LQ) in [23]. This detector is the MIMO version of the aforementioned NMF; thus, it can also be termed MIMO-NMF. It has been demonstrated to be able to keep constant the false alarm rate under different clutter distributions belonging to the compound Gaussian family, associated with each transmitter (TX) receiver (RX) pair. The mode of operation of the adopted detection rule is centralized.

In this work, we first discuss the received signal model for multistatic radar, where the target is observed in the presence of non-Gaussian disturbance. Then, two fundamental assumptions—uncorrelated channels and compound Gaussian disturbance—are introduced, in order to derive a suboptimum detection scheme, i.e. the

multichannel NMF. First, the performance of the proposed detector are tested by processing simulated data. The adaptive version of the adopted detector, i.e. the MIMO-NAMF is also implemented, by estimating the clutter covariance matrix [5]. The performance of the single-channel NAMF is then evaluated on real sea clutter data, collected by the nodes of the multistatic radar system, NetRAD [24, 25], in order to evaluate the differences between the bistatic and monostatic sea clutter from a radar detection standpoint. NetRAD sea clutter data have been analysed in some recent papers, in order to highlight the differences in the statistics between monostatic and bistatic sea clutter, which have been defined as *clutter diversity* in [25]. Our performance analysis aims at assessing which of the two channels is the more favourable for target detection. At the same time, the performance of the multichannel NAMF are also analysed by processing real clutter data, with the aim of investigating whether and under which conditions a multistatic detector is able to provide a performance gain with respect to the single-channel detector. In synthesis, the novelty of this work consists of the evaluation of false alarm regulation and detection performance over the two channels, bistatic and monostatic, with different statistical properties. Performance analysis has been carried out by processing both simulated and real clutter data.

The rest of this paper is organized as follows. In Section 2, we summarize the single-channel NMF detector, describe the multistatic signal model and derive the multichannel detection scheme. In Section 3, the performance of the multichannel NAMF are analysed by processing simulated data. In Section 4, the performance of the single-channel and multichannel NAMF are analysed by processing real sea clutter data collected by the NetRAD system. Final remarks are drawn in Section 5.

2 Problem formulation
2.1 Single-channel detection
In the case of single-channel radar, the received signal model under the hypothesis H_1 (target signal plus disturbance) is $\mathbf{z} = \alpha \mathbf{p} + \mathbf{w}$, whereas under the H_0 hypothesis (disturbance only), is $\mathbf{z} = \mathbf{w}$ ([1, 2]). The received signal samples, $z(n)$, are stacked into the vector $z = \{z(n)\}_{n=0}^{L-1}$, where L is the number of coherently integrated pulses. The time duration of the coherent processing interval (CPI) is T_{CPI}; thus, $L = T_{\mathrm{CPI}} \cdot \mathrm{PRF}$. Similarly, the vector $\mathbf{w}$ contains the disturbance samples. The target signal is modelled by the target complex amplitude α times the target steering vector $p = \{p(n)\}_{n=0}^{L-1}$, whose nth element is given by $p(n) = \exp\{-j2\pi n f_{\mathrm{D}}/\mathrm{PRF}\}$, where f_{D} is the target Doppler frequency.
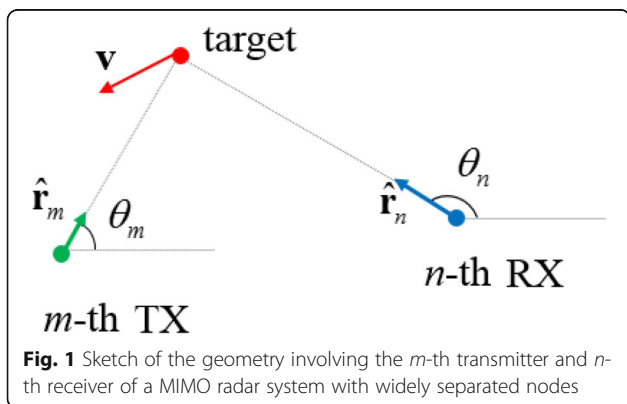
The disturbance is usually modelled as a compound Gaussian (CG) random vector, consisting of a slowly varying component, called texture, τ (assumed as completely correlated within a CPI), and a rapidly varying component, called speckle, $\mathbf{x}$; thus, $\boldsymbol{w} = \sqrt{\tau}\boldsymbol{x}$. The validity of this model for sea clutter has been discussed by a large number of works in literature for both monostatic [26–28] and, more recently, for bistatic clutter [25, 29, 30]. The rapid fluctuations of sea clutter are taken into account for the speckle component, which is modelled as a complex Gaussian random vector, whose covariance matrix is $\mathbf{R} = E\{\boldsymbol{x}\boldsymbol{x}^H\}$. As shown in many works (see, e.g. [1–3]), the NMF performs the following test:

$$\Lambda(\mathbf{z}) = \frac{\left|\mathbf{p}^H\mathbf{R}^{-1}\mathbf{z}\right|^2}{\left(\mathbf{p}^H\mathbf{R}^{-1}\mathbf{p}\right)\left(\mathbf{z}^H\mathbf{R}^{-1}\mathbf{z}\right)} \underset{H_0}{\overset{H_1}{\gtrless}} \eta. \tag{1}$$

The non-adaptive version requires the prior knowledge of the speckle covariance matrix, $\mathbf{R}$, whereas in the adaptive version, $\mathbf{R}$ is replaced by its estimate, $\hat{\mathbf{R}}$; in this case, the detector is called normalized adaptive matched filter (NAMF). This test has been demonstrated to be "texture-CFAR" and "covariance matrix-CFAR," i.e. it keeps constant the false alarm rate with respect to the texture distribution and to the shape of the speckle covariance matrix, if a proper estimation technique is used [4, 5, 31]. The estimation of the speckle covariance matrix is a crucial operation in order to guarantee good performance of the NAMF detector. In the case of CG-distributed clutter, the fixed-point (FP) estimate of the covariance matrix has been demonstrated [4–6] to be asymptotically optimum. Other possible estimators are the sample covariance matrix (SCM) and the normalized sample covariance matrix (NSCM) [32, 33].

2.2 Multichannel received signal model

Let us consider a radar system consisting of M transmitters and N receivers, whose geometry is sketched in Fig. 1. The transmitter and receiver indexes are m and n,

Fig. 1 Sketch of the geometry involving the *m*-th transmitter and *n*-th receiver of a MIMO radar system with widely separated nodes

respectively; thus, $m = 1,...,M$ and $n = 1,...,N$. The azimuth pointing angles of the m-th transmitter and n-th receiver are $\theta_m^{(t)}$ and $\theta_n^{(r)}$, respectively. The unit vector associated with the line-of-sight (LOS) of the m-th transmitter is $\mathbf{r}_m^{(t)}$, whereas $\mathbf{r}_n^{(t)}$ is the unit vector associated with the LOS of the n-th receiver. By assuming a bi-dimensional system geometry, the unit vectors are given by $\mathbf{r}_m^{(t)} = \begin{bmatrix} \cos\theta_m^{(t)} & \sin\theta_m^{(t)} \end{bmatrix}$ and $\mathbf{r}_n^{(r)} = \begin{bmatrix} \cos\theta_n^{(r)} & \sin\theta_n^{(r)} \end{bmatrix}$. The target velocity $\mathbf{v}$ consists of two components, v_x and v_y, i.e. $\mathbf{v} = [v_x \ v_y]$. Hence, the target Doppler frequency, associated with the mn-th TX-RX pair, is given by

$$\begin{aligned} f_D^{(mn)} &= \frac{1}{\lambda_0}\left(\mathbf{v}\cdot\mathbf{r}_m^{(t)} + \mathbf{v}\cdot\mathbf{r}_n^{(r)}\right) \\ &= \frac{1}{\lambda_0}\Big(v_x\cos\theta_m^{(t)} + v_x\cos\theta_n^{(r)} + v_y\sin\theta_m^{(t)} \\ &\quad + v_y\sin\theta_n^{(r)}\Big) \end{aligned} \tag{2}$$

The signal received by the nth receiver and transmitted by the m-th transmitter is indicated as $z_{mn}(l)$, where l is the pulse index. We assume that the CPI consists of L samples, assumed equal for all the TX-RX pairs; thus, the received signal vector can be expressed as $\mathbf{z}_{mn} = \{z_{mn}(l)\}_{l=0}^{L-1}$. We can distinguish between the H_1 and the H_0 hypotheses:

$$\begin{aligned} H_1 &: \mathbf{z}_{m,n} = \alpha_{m,n}\mathbf{p}_{m,n} + \mathbf{w}_{m,n}, \\ H_0 &: \mathbf{z}_{m,n} = \mathbf{w}_{m,n}, \end{aligned} \tag{3}$$

where $m = 1, ..., M$ $n = 1, ..., N$, α_{mn} is the target complex amplitude and $\mathbf{w}_{mn}$ is the disturbance. A general received signal model is obtained by stacking the vectors $\mathbf{z}_{mn}$ for all the TX-RX pairs, i.e. $\mathbf{z} = [\mathbf{z}_{11}^T, ..., \mathbf{z}_{1N}^T, \mathbf{z}_{21}^T, ..., \mathbf{z}_{2N}^T, ..., \mathbf{z}_{M1}^T, ..., \mathbf{z}_{MN}^T]^T$, and then,

$$\begin{aligned} H_1 &: \quad \mathbf{z} = \mathbf{P}\boldsymbol{\alpha} + \mathbf{w}, \\ H_0 &: \quad \mathbf{z} = \mathbf{w}, \end{aligned} \tag{4}$$

where $\mathbf{P} = \text{diag}\big([\mathbf{p}_{11}^T, ..., \mathbf{p}_{MN}^T]\big)$, $\mathbf{w} = [\mathbf{w}_{11}^T, ..., \mathbf{w}_{MN}^T]^T$. In a more general case, the disturbance can be modelled as a complex elliptically symmetric (CES) random variable [34], and then, its multivariate probability density function (pdf) can be expressed as

$$f_{\mathbf{W}}(\mathbf{w}) = C_{L,g}|\boldsymbol{\Sigma}|^{-1}g\big(\mathbf{w}^H\boldsymbol{\Sigma}^{-1}\mathbf{w}\big) \tag{5}$$

where $g(.)$ is the density generator, $\boldsymbol{\Sigma}$ is the covariance matrix and $C_{L,g}$ is the normalizing constant [34]. The compound Gaussian family is a subset of the CES family, described by the following density generator:

Palamà *et al. EURASIP Journal on Advances in Signal Processing* (2016) 2016:107

Page 4 of 17

$$g(t) = \int_0^\infty \tau^{-L} \exp\{-t/\tau\} f_\tau(\tau) d\tau, \qquad (6)$$

and normalizing constant $C_{L,g} = \pi^{-L}$. The texture is distributed according to $f_\tau(\tau)$.

In the multidimensional disturbance model, there is a combination of a multidimensional texture vector $\boldsymbol{\tau} = [\tau_{11}(0) \dots \tau_{11}(L-1) \dots \tau_{MN}(0) \dots \tau_{MN}(L-1)]^T$ and speckle vector $\mathbf{s} = [s_{11}(0) \dots s_{11}(L-1), \dots, s_{MN}(0) \dots s_{MN}(L-1)]$. Hence, the disturbance $\mathbf{w}$ can be expressed as

$$\mathbf{w} = \boldsymbol{\tau}^{1/2} \odot \mathbf{s} = \mathbf{Ts} \qquad (7)$$

where $\odot$ denotes the Hadamard product and $\mathbf{T}$ is a diagonal matrix, containing the texture samples, $\mathbf{T} = \text{diag}(\boldsymbol{\tau}^{1/2})$. The space-time clutter covariance matrix, $\boldsymbol{\Sigma}$, is given by

$$\begin{aligned} \boldsymbol{\Sigma} &= E\{\mathbf{w}\mathbf{w}^H\} = E\{\mathbf{T}\mathbf{s}\mathbf{s}^H\mathbf{T}^H\} = E\left\{\left(\boldsymbol{\tau}^{1/2}\odot\mathbf{s}\right)\left(\boldsymbol{\tau}^{1/2}\odot\mathbf{s}\right)^H\right\} \\ &= E\left\{\boldsymbol{\tau}^{1/2}\left(\boldsymbol{\tau}^{1/2}\right)^H\right\} \odot E\{\mathbf{s}\mathbf{s}^H\} = \mathbf{C}^{1/2}\odot\mathbf{R} \end{aligned}$$
$$(8)$$

where $\mathbf{R}$ is the space-time speckle covariance matrix and $\mathbf{C}$ is the space-time covariance matrix of the texture. It can be concluded that the global covariance matrix $\boldsymbol{\Sigma}$ is given by the Hadamard (i.e. element-wise) product of the space-time speckle and texture covariance matrices. The size of $\boldsymbol{\Sigma}$, $\mathbf{R}$ and $\mathbf{C}$ is $MNL \times MNL$, i.e. the product of the number of TX-RX pairs (MN) times the number of integrated pulses, L. Each space-time covariance matrix can be viewed as a block-matrix, whose block size is $L \times L$ and total number of blocks is $(MN)^2$. The global, speckle and texture covariance matrices are related by

$$\begin{aligned} &\begin{bmatrix} \boldsymbol{\Sigma}_{1,1} & \cdots & \boldsymbol{\Sigma}_{1,MN} \\ \vdots & \ddots & \vdots \\ \boldsymbol{\Sigma}_{MN,1} & \cdots & \boldsymbol{\Sigma}_{MN,MN} \end{bmatrix} = \begin{bmatrix} \mathbf{C}_{1,1}^{1/2} & \cdots & \mathbf{C}_{1,MN}^{1/2} \\ \vdots & \ddots & \vdots \\ \mathbf{C}_{MN,1}^{1/2} & \cdots & \mathbf{C}_{MN,MN}^{1/2} \end{bmatrix} \\ &\odot \begin{bmatrix} \mathbf{R}_{1,1} & \cdots & \mathbf{R}_{1,MN} \\ \vdots & \ddots & \vdots \\ \mathbf{R}_{MN,1} & \cdots & \mathbf{R}_{MN,MN} \end{bmatrix} \\ &= \begin{bmatrix} \mathbf{C}_{1,1}^{1/2}\odot\mathbf{R}_{1,1} & \cdots & \mathbf{C}_{1,MN}^{1/2}\odot\mathbf{R}_{1,MN} \\ \vdots & \ddots & \vdots \\ \mathbf{C}_{MN,1}^{1/2}\odot\mathbf{R}_{MN,1} & \cdots & \mathbf{C}_{MN,MN}^{1/2}\odot\mathbf{R}_{MN,MN} \end{bmatrix} \end{aligned}$$
$$(9)$$

The general blocks $\boldsymbol{\Sigma}_{mn,rs}$, $\mathbf{C}_{mn,rs}$ and $\mathbf{R}_{mn,rs}$ are given by

$$\begin{cases} \boldsymbol{\Sigma}_{mn,rs} = E\{\mathbf{w}_{mn}\mathbf{w}_{rs}^H\} \\ \mathbf{C}_{mn,rs} = E\{\boldsymbol{\tau}_{mn}\boldsymbol{\tau}_{rs}^H\} \\ \mathbf{R}_{mn,rs} = E\{\mathbf{s}_{mn}\mathbf{s}_{rs}^H\} \end{cases}$$
$$(10)$$

$m, r = 1, \dots, M$; $n, s = 1, \dots, N$. By examining Eq. (9), it could be noted that the blocks on the main diagonal represent the autocovariance matrices of the clutter, texture and speckle samples collected by one transmitter-receiver pair, whereas the blocks off the diagonal represent the cross-covariances between the temporal samples collected by the mn-th and rs-th channels. Hence, if the channels are assumed statistically independent, matrices $\boldsymbol{\Sigma}$, $\mathbf{C}$, and $\mathbf{R}$ are block-diagonal. Due to the element-wise product structure shown in (9), in order for the global space-time covariance matrix to be not block-diagonal, both the texture covariance matrix, $\mathbf{C}$, and speckle covariance matrix, $\mathbf{R}$, should not be block-diagonal. In other words, both the texture and speckle samples should be correlated across different TX-RX pairs. However, in this work, the channels are assumed statistically independent; hence, the matrices $\boldsymbol{\Sigma}$, $\mathbf{C}$ and $\mathbf{R}$ are block-diagonal.[1]

The target complex amplitudes can be stacked into the vector $\boldsymbol{\alpha}$, whose covariance matrix is $\mathbf{C}_\alpha = E\{\boldsymbol{\alpha}\boldsymbol{\alpha}^H\}$, of size $MNL \times MNL$, and is block-structured, similar to $\boldsymbol{\Sigma}$, $\mathbf{C}$ and $\mathbf{R}$. Hence, if the target returns are statistically independent across different channels, the matrix $\mathbf{C}_\alpha$ is block-diagonal. In addition, if a Swerling I target model is used, the target amplitude is constant within a CPI.

Under the assumption of compound Gaussian clutter, the joint pdfs under the hypotheses H_0 and H_1 are given by [34]

$$f(\mathbf{z}|H_0) = \int f(\mathbf{z}|H_0, \boldsymbol{\tau}_0) f(\boldsymbol{\tau}_0) d\boldsymbol{\tau}_0 \qquad (11)$$

$$f(\mathbf{z}|H_1, \boldsymbol{\alpha}, \mathbf{v}) = \int f(\mathbf{z}|H_1, \boldsymbol{\alpha}, \mathbf{v}, \boldsymbol{\tau}_1) f(\boldsymbol{\tau}_1) d\boldsymbol{\tau}_1 \qquad (12)$$

where the vectors $\boldsymbol{\tau}_0$ and $\boldsymbol{\tau}_1$ are the texture vectors in the two hypotheses.

Under the assumption of independent channels, concerning both the clutter and target returns, the joint pdfs can be written as:

$$\begin{aligned} f(\mathbf{z}|H_0) &= \prod_{m=1}^M \prod_{n=1}^N f(\mathbf{z}_{m,n}|H_0) \\ &= \prod_{m=1}^M \prod_{n=1}^N \int f\left(\mathbf{z}_{m,n}\Big|H_0, \tau_{m,n}^{(0)}\right) f\left(\tau_{m,n}^{(0)}\right) d\tau_{m,n}^{(0)} \end{aligned}$$
$$(13)$$

$$f(\mathbf{z}|H_1,\boldsymbol{\alpha},\mathbf{v}) = \prod_{m=1}^{M}\prod_{n=1}^{N} f(\mathbf{z}_{m,n}|H_1,\alpha_{m,n},\mathbf{v})$$

$$= \prod_{m=1}^{M}\prod_{n=1}^{N} \int f\left(\mathbf{z}_{m,n}\Big|H_1,\tau_{m,n}^{(1)},\alpha_{m,n},\mathbf{v}\right) f\left(\tau_{m,n}^{(1)}\right) d\tau_{m,n}^{(1)}$$

(14)

where

$$f\left(\mathbf{z}_{m,n}|H_0\right) = \frac{g_{m,n}^{(0)}\left(q_{m,n}^{(0)}(\mathbf{z}_{m,n})\right)}{\pi^L|\mathbf{M}_{m,n}|}$$

$$= \frac{1}{\pi^L|\mathbf{M}_{m,n}|} \int_0^\infty \left[\tau_{m,n}^{(0)}\right]^{-L}$$

$$\exp\left\{\frac{-q_{m,n}^{(0)}(\mathbf{z}_{m,n})}{2\tau_{m,n}^{(0)}}\right\} f\left(\tau_{m,n}^{(0)}\right) d\tau_{m,n}^{(0)}$$

(15)

$$f\left(\mathbf{z}_{m,n}|H_1,\alpha_{m,n},v_x,v_y\right) = \frac{g_{m,n}^{(1)}\left(q_{m,n}^{(1)}(\mathbf{z}_{m,n})\right)}{\pi^L|\mathbf{M}_{m,n}|}$$

$$= \frac{1}{\pi^L|\mathbf{M}_{m,n}|} \int_0^\infty \left[\tau_{m,n}^{(1)}\right]^{-L}$$

$$\exp\left\{-\frac{q_{m,n}^{(1)}(\mathbf{z}_{m,n})}{2\tau_{m,n}^{(1)}}\right\} f\left(\tau_{m,n}^{(1)}\right) d\tau_{m,n}^{(1)}$$

(16)

In the general case of CG disturbance, the expressions of the joint pdfs (11)–(12) have not closed form; thus, the optimum detector cannot be derived in closed form. A suboptimum approach [2] consists of replacing the texture with its maximum likelihood estimate (MLE), which gives the following GLRT:

$$\frac{\Lambda(\mathbf{z}) = \max_{\tau_1,\boldsymbol{\alpha},\mathbf{v}} f(\mathbf{z}|H_1,\boldsymbol{\alpha},\mathbf{v},\tau_1)}{\max_{\tau_0} f(\mathbf{z}|H_0,\tau_0)} \underset{H_0}{\overset{H_1}{\underset{>}{\gtrless}}} \lambda \quad (17)$$

This approach is tantamount to consider the clutter as Gaussian distributed with unknown covariance. In the following, a multichannel GLRT is derived in both cases of perfectly known target signal and unknown target complex amplitude.

2.3 Multichannel detection

In the case that target signal is perfectly known, we have knowledge of the elements of the vector $\boldsymbol{\alpha}$ containing the target complex amplitudes and of the target steering vectors $\mathbf{p}_{mn}$, for all the values of m and n, which in turn requires a perfect knowledge of the system geometry and of the target velocity $\mathbf{v}$. Hence, the target signal, for the mnth pair, is $\mathbf{s}_{m,n} = \alpha_{m,n}\mathbf{p}_{m,n}$; thus, $q_{m,n}^{(1)}(\mathbf{z}_{m,n}) = \left(\mathbf{z}_{m,n}-\mathbf{s}_{m,n}\right)^H\mathbf{R}_{m,n}^{-1}\left(\mathbf{z}_{m,n}-\mathbf{s}_{m,n}\right)$.

The GLRT reduces to

$$\Lambda(\mathbf{z}) = \frac{\max_{\tau_1} f(\mathbf{z}|H_1,\tau_1)}{\max_{\tau_0} f(\mathbf{z}|H_0,\tau_0)} \underset{H_0}{\overset{H_1}{\underset{<}{\gtrless}}} \lambda \quad (18)$$

The numerator is $\max_{\tau_1} f(\mathbf{z}|H_1,\tau_1) = f(\mathbf{z}|H_1,\hat{\tau}_1)$, where $\hat{\tau}_1$ is the texture MLE, which can be calculated as $\nabla_{\tau_1}\{f(\mathbf{z}|H_1,\tau_1)\}|_{\tau_1=\hat{\tau}_1} = 0$. In the case that the clutter samples are statistically independent across channels, we have $\partial f(\mathbf{z}|H_1,\tau_1)/\partial\tau_{mn}^{(1)} = \partial f(z_{mn}|H_1,\tau_{mn}^{(1)})/\partial\tau_{mn}^{(1)}$. The texture MLE for the mnth channel, $\hat{\tau}_{mn}$, is obtained by equating to zero the previous derivative. Hence, the vector consists of the texture estimates, calculated separately for each receiver-transmitter pair. $\hat{\boldsymbol{\tau}}_1 = \left\{\hat{\tau}_{m,n}^{(1)}\right\}_{m,n=1,1}^{M,N} = \left[\hat{\tau}_{1,1}^{(1)}...\hat{\tau}_{M,N}^{(1)}\right]$, where

$$\hat{\tau}_{m,n}^{(1)} = \underset{\tau_{m,n}^{(1)}}{\arg\max}\left\{f\left(\mathbf{z}_{m,n}\Big|H_1,\tau_{m,n}^{(1)}\right)\right\}$$

$$= \frac{q_{m,n}^{(1)}(\mathbf{z}_{m,n})}{2L} \quad (19)$$

thus,

$$f\left(\mathbf{z}_{m,n}\Big|H_1,\hat{\tau}_{m,n}^{(1)}\right) = \frac{1}{\pi^L|\mathbf{R}_{m,n}|}\left[\hat{\tau}_{m,n}^{(1)}\right]^{-L}\exp\left\{\frac{-q_{m,n}^{(1)}(\mathbf{z}_{m,n})}{2\hat{\tau}_{m,n}^{(1)}}\right\}$$

$$= \frac{1}{\pi^L|\mathbf{R}_{m,n}|}\left[\frac{q_{m,n}^{(1)}(\mathbf{z}_{m,n})}{2L}\right]^{-L} e^{-L/2}$$

(20)

Similarly, under the H_0 hypothesis, the texture MLE for the mnth channel is $\hat{\tau}_{m,n}^{(0)} = q_{m,n}^{(0)}(\mathbf{z}_{m,n})/2L$; thus,

$$f\left(\mathbf{z}_{m,n}\Big|H_0,\hat{\tau}_{m,n}^{(0)}\right) = \frac{1}{\pi^L|\mathbf{R}_{m,n}|}\left[\frac{q_{m,n}^{(0)}(\mathbf{z}_{m,n})}{2L}\right]^{-L} e^{-L/2}.$$

(21)

The suboptimum GLR in (18) is given by

$$\Lambda(\mathbf{z}) = \prod_{m=1}^{M}\prod_{n=1}^{N}\frac{f\left(\mathbf{z}_{m,n}\Big|H_1,\hat{\tau}_{m,n}^{(1)}\right)}{f\left(\mathbf{z}_{m,n}\Big|H_0,\hat{\tau}_{m,n}^{(0)}\right)} = \prod_{m=1}^{M}\prod_{n=1}^{N}\left[\frac{\tau_{m,n}^{(0)}}{\tau_{m,n}^{(1)}}\right]^L$$

$$= \prod_{m=1}^{M}\prod_{n=1}^{N}\left[\frac{q_{m,n}^{(0)}}{q_{m,n}^{(1)}}\right]^L = \prod_{m=1}^{M}\prod_{n=1}^{N}\left(1 + \frac{q_{m,n}^{(1)}-q_{m,n}^{(0)}}{q_{m,n}^{(0)}}\right)^{-L}$$

$$= \prod_{m=1}^{M}\prod_{n=1}^{N}\left(1 + \frac{-2\mathrm{Re}\left\{\mathbf{s}_{m,n}^H\mathbf{R}_{m,n}^{-1}\mathbf{z}_{m,n}\right\} + \mathbf{s}_{m,n}^H\mathbf{R}_{m,n}^{-1}\mathbf{s}_{m,n}}{\mathbf{z}_{m,n}^H\mathbf{R}_{m,n}^{-1}\mathbf{z}_{m,n}}\right)^{-L}$$

(22)

Palamà *et al. EURASIP Journal on Advances in Signal Processing* (2016) 2016:107

Page 6 of 17

Hence, the suboptimum multichannel GLRT for perfectly known signal can be recast as

$$\Lambda(\mathbf{z}) = \prod_{m=1}^{M}\prod_{n=1}^{N}\left(1 - \frac{2\mathrm{Re}\left\{\mathbf{s}_{m,n}^{H}\mathbf{R}_{m,n}^{-1}\mathbf{z}_{m,n}\right\} - \mathbf{s}_{m,n}^{H}\mathbf{R}_{m,n}^{-1}\mathbf{s}_{m,n}}{\mathbf{z}_{m,n}^{H}\mathbf{R}_{m,n}^{-1}\mathbf{z}_{m,n}}\right)^{-1} \overset{H_1}{\underset{H_0}{\gtrless}} \lambda \quad (23)$$

In the case that the target complex amplitudes, contained in the vector $\boldsymbol{\alpha}$, are now unknown parameters (and the target velocity $\mathbf{v}$ is still a known quantity), the general form of the adopted suboptimum GLRT is given by

$$\frac{\Lambda(\mathbf{z}) = \max_{\boldsymbol{\alpha},\boldsymbol{\tau}_1} f(\mathbf{z}|H_1,\boldsymbol{\alpha},\boldsymbol{\tau}_1)}{\max_{\boldsymbol{\tau}_0} f(\mathbf{z}|H_0,\boldsymbol{\tau}_0)} \overset{H_1}{\underset{H_0}{\gtrless}} \lambda. \quad (24)$$

Due to the statistical independence across the target returns associated with different channels, the MLE of the vector $\boldsymbol{\alpha}$ is a vector consisting of the MLEs of the target complex amplitude associated with all the TX-RX pairs ($\hat{\alpha}_{m,n}$, $m = 1,\dots,M$ and $n = 1,\dots,N$), i.e. $\hat{\boldsymbol{\alpha}} = \{\hat{\alpha_{m,n}}\}_{m,n=1,1}^{M,N}$; thus, for the mn-th channel,

$$\begin{aligned}\hat{\alpha}_{m,n} &= \underset{\alpha_{m,n}}{\arg\max}\left\{f_{m,n}\left(\mathbf{z}_{m,n}\Big|H_1,\hat{\tau}_{m,n}^{(1)}\right)\right\}\\ &= \underset{\alpha_{m,n}}{\arg\max}\left\{\frac{1}{\pi^L|\mathbf{R}_{m,n}|}\left[\frac{q_{m,n}^{(1)}(\mathbf{z}_{m,n})}{2L}\right]^{-L}\exp\left(-\frac{L}{2}\right)\right\}\\ &= \underset{\alpha_{m,n}}{\arg\max}\left\{\left[q_{m,n}^{(1)}(\mathbf{z}_{m,n})\right]^{-L}\right\}\\ &= \underset{\alpha_{m,n}}{\arg\max}\left\{\left[(\mathbf{z}_{m,n}-\alpha_{m,n}\mathbf{p}_{m,n})^H\mathbf{R}_{m,n}^{-1}(\mathbf{z}_{m,n}-\alpha_{m,n}\mathbf{p}_{m,n})\right]^{-L}\right\}\end{aligned} \quad (25)$$

After straightforward manipulations, the value of α_{mn} that maximizes the final quantity in (25) is

$$\hat{\alpha}_{m,n} = \frac{\mathbf{p}_{m,n}^H\mathbf{R}_{m,n}^{-1}\mathbf{z}_{m,n}}{\mathbf{p}_{m,n}^H\mathbf{R}_{m,n}^{-1}\mathbf{p}_{m,n}} \quad (26)$$

By substituting the value of $\hat{\alpha}_{mn}$ in the general expression of the suboptimum GLRT in (22), we obtain

Hence, the multichannel GLRT in the case of unknown complex target amplitude can be recast in the form

$$\Lambda(\mathbf{z}) = \prod_{m=1}^{M}\prod_{n=1}^{N}\left[1 - \frac{\left|\mathbf{p}_{m,n}^H\mathbf{R}_{m,n}^{-1}\mathbf{z}_{m,n}\right|^2}{\left(\mathbf{p}_{m,n}^H\mathbf{R}_{m,n}^{-1}\mathbf{p}_{m,n}\right)\left(\mathbf{z}_{m,n}^H\mathbf{R}_{m,n}^{-1}\mathbf{z}_{m,n}\right)}\right]^{-1} \overset{H_1}{\underset{H_0}{\gtrless}} \lambda, \quad (28)$$

which is the MIMO (or *multichannel*) version of the normalized matched filter. This detector has been originally derived in [23] in a different manner. In [23], the authors show that in the case of known covariance matrices, this detector is texture-CFAR and P_{FA} is a function only of the detection threshold λ, the number of pulses L and the number of transmitter-receiver pairs ($MN = P$),

$$P_{FA} = \lambda^{1-L}\sum_{p=0}^{P-1}\frac{(L-1)^p}{p!}(\ln\lambda)^p. \quad (29)$$

If $P = 1$ (one receiver and one transmitter), $P_{FA} = \lambda^{1-L}$, which is the well-known expression of the probability of false alarm achieved by the *single-channel* NMF [1]. In [23], it is also shown that detector (28) outperforms the MIMO-Optimum Gaussian Detector (MIMO-OGD) in non-Gaussian clutter.

3 Performance analysis on simulated data

The performance of the multichannel NMF detector was analysed by simulating the target and clutter signals. Simulations were realized for both known and unknown covariance matrix. In the latter case, the adaptive version of the detector (28) was implemented, by replacing the covariance matrix with its estimates.

The global signal-to-clutter ratio (SCR) is given by the sum of all the local signal-to-clutter ratios (SCR_{mn}), $SCR = \sum_{m=1}^{M}\sum_{n=1}^{N}SCR_{mn}$, where the local SCR is given by

$$SCR_{mn} = \frac{P_{s^{(mn)}}}{P_{c^{(mn)}}} = \frac{E\{|\alpha_{mn}|^2\}}{2E\{\tau_{mn}\}} \quad (30)$$

In the simulations, SCR is assumed uniformly distributed over all the transmitter-receiver pairs; thus, $SCR_{mn} = SCR/MN$. The target is modelled according

$$\begin{aligned}\Lambda(\mathbf{z}) &= \prod_{m=1}^{M}\prod_{n=1}^{N}\left[1 + \frac{q_{m,n}^{(1)}-q_{m,n}^{(0)}}{q_{m,n}^{(0)}}\right]^{-L} = = \prod_{m=1}^{M}\prod_{n=1}^{N}\left[1 + \frac{-2Re\left\{\hat{\alpha}_{m,n}\mathbf{z}_{m,n}^H\mathbf{M}_{m,n}^{-1}\mathbf{p}_{m,n}\right\} + |\hat{\alpha}_{m,n}|^2\mathbf{p}_{m,n}^H\mathbf{M}_{m,n}^{-1}\mathbf{p}_{m,n}}{\mathbf{z}_{m,n}^H\mathbf{M}_{m,n}^{-1}\mathbf{z}_{m,n}}\right]^{-L}\\ &= \prod_{m=1}^{M}\prod_{n=1}^{N}\left[1 - \frac{\left|\mathbf{p}_{m,n}^H\mathbf{M}_{m,n}^{-1}\mathbf{z}_{m,n}\right|^2}{\left(\mathbf{p}_{m,n}^H\mathbf{M}_{m,n}^{-1}\mathbf{p}_{m,n}\right)\left(\mathbf{z}_{m,n}^H\mathbf{M}_{m,n}^{-1}\mathbf{z}_{m,n}\right)}\right]^{-L}\end{aligned}$$

$$(27)$$

Palamà *et al. EURASIP Journal on Advances in Signal Processing* (2016) 2016:107

Page 7 of 17

to the Swerling-I model, and its amplitude is a complex Gaussian random variable and independent for different TX-RX pairs. For each CPI, one value of the complex amplitude is generated, according to the complex Gaussian distribution, and assumed as constant for all the samples within the CPI. The clutter power $P_c^{(mn)}$ is assumed equal to 1. The clutter is modelled as a first-order autoregressive stochastic process, AR(1), characterized by the one-lag correlation coefficient ρ_{mn} and centre frequency $f_c^{(mn)}$ [35]. Both the target Doppler frequency and the clutter centre frequency were assumed to be zero, in order to remove the influence of the system geometry on the algorithm performance, and to consider the worst case, where the target is totally embedded in clutter. Then, we set $\rho_{mn} = 0.9$, a value that is typically adopted to model sea clutter spectrum. We considered the case of two TX-RX pairs, studying three different cases for the clutter statistical distribution, illustrated in Table 1 (note that the shape parameters are indicated as ν, with a subscript indicating the channel index, whereas $p^{(n)}$ indicates the noise level for the K-plus-noise distribution). In the case of K-plus-noise distribution, the clutter-to-noise ratio (CNR) is also indicated in Table 1. The number of integrated pulses, L, was set equal to 8. We considered both the scenarios where the speckle covariance matrix is known and unknown (and estimated by using the SCM, NSCM and FP estimates). The number of iterations for the iterative estimation algorithm was set to 4. The number of Monte Carlo runs was 10^7. The number of secondary range cells used to estimate the clutter covariance matrix was $K = 2L$, which guarantees quite accurate covariance estimates [5].

3.1 False alarm regulation
The false alarm regulation performance of the multichannel NMF detector, (28), is illustrated in Fig. 2. The P_{FA} values obtained by simulating the clutter samples, and using the statistical models described in Table 1, are compared with the theoretical P_{FA} values, given by (29) [23]. In the case of known covariance matrix, the P_{FA} values are identical for all the clutter configurations, perfectly matched with the theoretical values; thus, the

CFAR property of the multichannel NMF in the ideal case (i.e. non-adaptive) is confirmed. The P_{FA} values are not influenced by the clutter distribution, if the covariance matrix is estimated by the NSCM and FP methods, which indeed confirms the robustness of the multichannel NAMF. On the other hand, the multichannel NAMF that utilizes the SCM covariance estimate is not a CFAR detector with respect to the clutter distribution. These results are expected, as the SCM estimator is optimum in the case of Gaussian clutter, whereas the NSCM and FP estimators are able to give good estimates in the case of compound Gaussian clutter [4–6].

By evaluating the "P_{FA}-vs-threshold" plots, the values of the detection threshold λ can be set in order to achieve a desired value of the P_{FA}. As the values of λ depends on the technique used to estimate the covariance matrix, λ_{KC} indicates the value of the threshold in the case of known covariance matrix; λ_{NSCM} and λ_{FP} are the values of the threshold in the case of NSCM and FP estimates, respectively. The values of λ_{KC}, λ_{NSCM} and λ_{FP} to set in order to achieve P_{FA} values from 10^{-5} to 10^{-2} are shown in Table 3. These values will be used in evaluating the detection performance of the multichannel NAMF, by setting a desired P_{FA}.

3.2 Detection performance
The ROC of the multichannel NAMF have been derived for the three clutter configurations illustrated in Table 1; for known and estimated covariance matrix, the global SCR was equal to 10 dB. Figure 3 shows the ROC curves of the MIMO-NAMF, i.e. for unknown target signal.
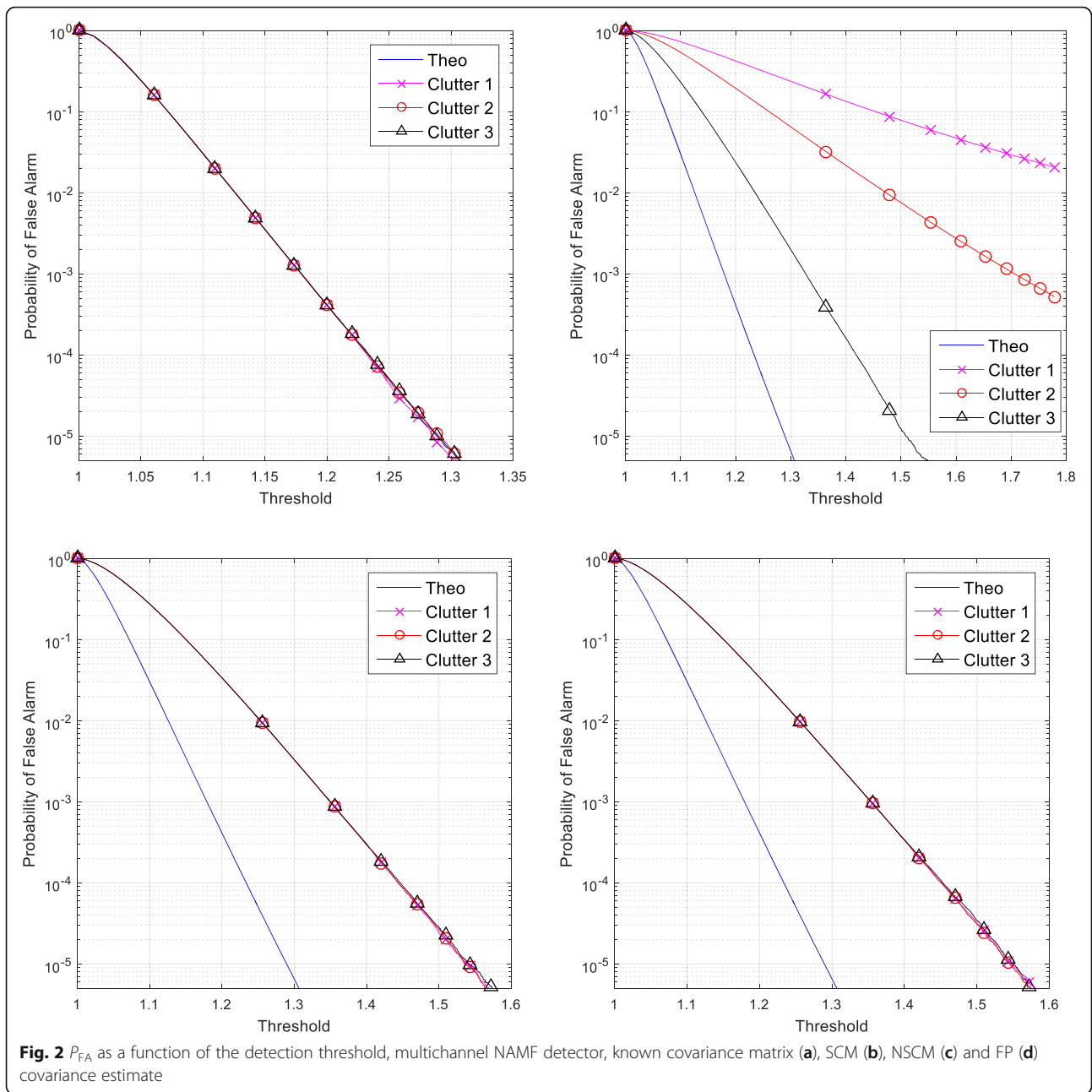
The detection performance in the first clutter configuration is similar to the one in the second clutter configuration, whereas it decreases in the third clutter configuration. This is probably because the third clutter configuration includes the presence of a thermal noise component. The P_D values are, as expected, the highest in the case of known covariance matrix. Furthermore, the NSCM method shows slightly better performance than the FP, whereas the P_D values obtained through the SCM method are always lower than the one obtained by using the NSCM and FP methods. This is an expected result, because the SCM method is optimum only if the clutter is Gaussian.

It should be noted that the single-channel optimum detector has already shown (for many combinations of the values of P_{FA} and SCR) better detection performance with decreasing values of the K-distribution shape parameter, i.e. with increasing clutter spikiness [1, 33, 38–40]

The ROC curves have shown that different shape parameter values associated with different TX-RX pairs have an impact on the detection performance. In order to better evaluate this impact, simulations were realized
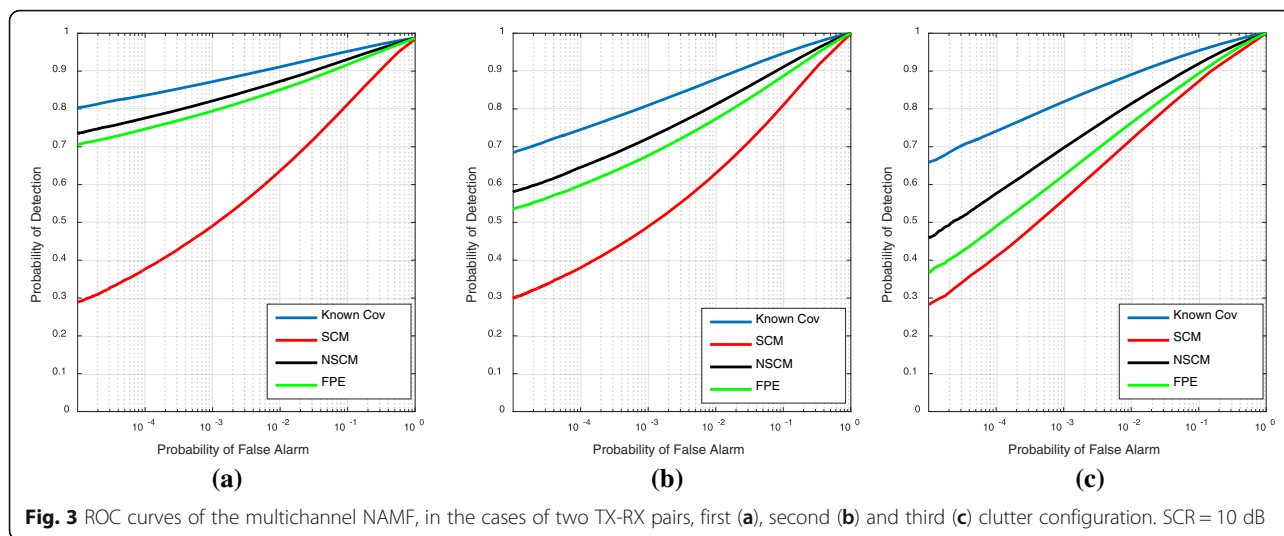
Table 1 Clutter configurations

Clutter configuration	Statistical distribution	Parameters
1	K	$\nu_1 = 0.1$, $\nu_2 = 0.5$
2	K	$\nu_1 = 0.2$, $\nu_2 = 0.9$
3	K-plus-noise	$\nu_1 = 0.2$, $\nu_2 = 0.9$
		$p_1^{(n)} = p_2^{(n)} = 0.1$
		CNR = 10 dB

Palamà *et al. EURASIP Journal on Advances in Signal Processing* (2016) 2016:107

Page 8 of 17

Fig. 2 P_{FA} as a function of the detection threshold, multichannel NAMF detector, known covariance matrix (**a**), SCM (**b**), NSCM (**c**) and FP (**d**) covariance estimate

by generating clutter samples distributed according to the K-plus-noise distribution, with unitary clutter power, thermal noise power of 0.1 and different values of the shape parameters (v_1, v_2), both included between 0.04 and 1.2 (in real data, the values of the shape parameter are usually included within this interval [30]). The threshold values were set in order to obtain a $P_{FA} = 10^{-5}$, as shown in Table 2. P_D was calculated for each pair of shape parameters (v_1, v_2). Figure 4 shows 3D contour plots of the P_D values versus (v_1, v_2), for a value of the global SCR of 15 dB. A peak occurs for both the shape parameters equal to about 0.15, which is suggested by

the black contours (delimiting the areas where $P_D \geq 0.93$) in Fig. 4a, red contours ($P_D \geq 0.93$) in Fig. 4b, and by the orange contour in Fig. 4c (delimiting the area where $P_D \geq 0.85$). For both the shape parameters greater than 0.1, the contour plots are similar to hyperbolas, meaning that high P_D values are obtained for low values of the shape parameters. It could be noted that the gradient (through which the values of P_D decrease with increasing either v_1 or v_2) is less steep in the case of known covariance matrix with respect to the cases of unknown estimated covariance matrix. The SCM estimator has not been considered for this analysis, as it has already

Palamà *et al. EURASIP Journal on Advances in Signal Processing* (2016) 2016:107

Page 9 of 17

Fig. 3 ROC curves of the multichannel NAMF, in the cases of two TX-RX pairs, first (**a**), second (**b**) and third (**c**) clutter configuration. SCR = 10 dB

shown much lower performance than the NSCM and FP estimators. In addition, the NSCM covariance estimator shows better performance than the FP one and a less steep gradient. The contour plots highlight that identical values of P_D are achieved by the multichannel NAMF for different combinations of the shape parameters associated with the two jointly processed channels. In other words, the clutter conditions experienced by each of the two channels jointly influence the global detection performance.

In recent works [25, 30], the statistical analysis of simultaneously collected bistatic and monostatic data of the shape parameter has highlighted that the monostatic shape parameter is almost constant with range, whereas the bistatic one shows large deviations, due to the geometry change. Hence, the detection performance, achieved by applying the multichannel NAMF to monostatic and bistatic data at different ranges, may be heavily influenced by this clutter diversity, especially by the behaviour of bistatic clutter.

4 Performance analysis on real data
4.1 Data overview
The performance of the multichannel NAMF were analysed on real sea clutter data, collected by the nodes of the NetRAD system, which is an S-band multistatic radar system, developed at the University College London. The
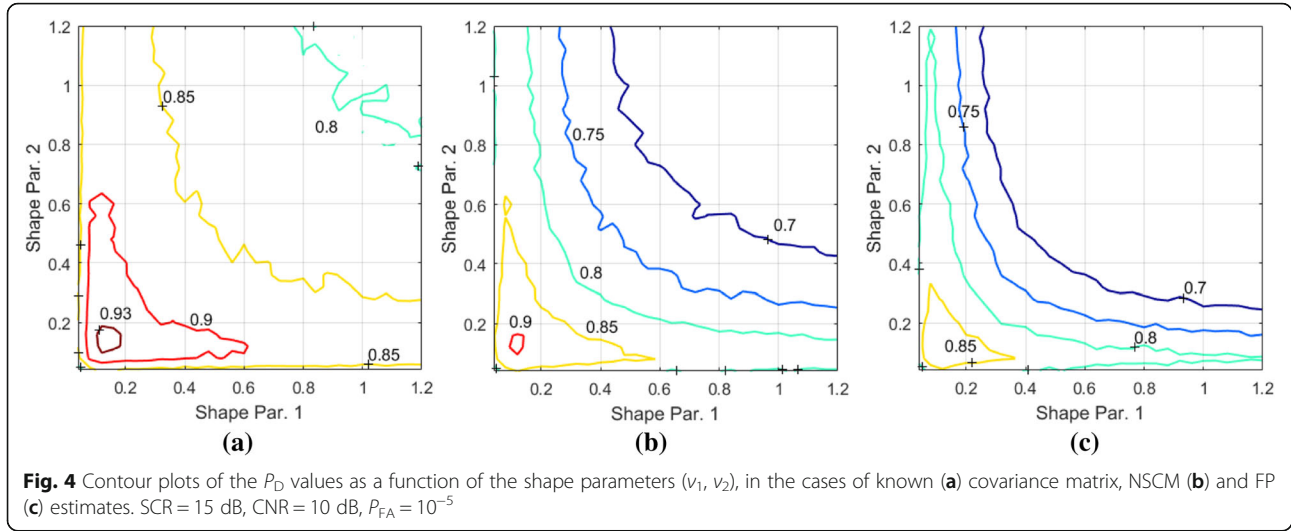
main parameters of the NetRAD are summarized in Table 3.

The analysed data were collected by the NetRAD system during a measurement campaign realized in October 2010 at Scarborough, Cape Town, by researchers from the University College London and University of Cape Town. Two nodes—a monostatic one and a bistatic one—were employed in the measurements and were located on the sea coast, at a short distance from the sea.

Measurements were made by varying the azimuth angle, polarization and baseline. For each range cell, the number of received pulses is $N_p = 130,000$, corresponding to a total acquisition time of 130 s. In this work, we consider the datasets collected on October 21, 2010, with a baseline of 728 m and a bistatic angle (β) of 30° [25, 30].

In order to evaluate the performance of both single-channel and multichannel NAMF detectors on NetRAD data, a target was simulated and its signal superimposed on real clutter data. In particular, the target fluctuations were modelled according to the Swerling-I model, with a complex Gaussian target amplitude, completely correlated within a CPI. The signal-to-clutter ratio (SCR) was set similar to the case of simulated data, and the clutter power is directly computed from the data [30].

The target Doppler frequency, f_D, influences heavily the performance of a detection algorithm, as if the Range-Doppler bin of the target is located within an area of low clutter power, the detection performance will be high. In order to evaluate the impact of sea clutter on false alarm regulation and on detection performance, the range cell under test (r_{CUT}) was set where the clutter power is high for both the bistatic and monostatic sea clutter data, i.e. at the centre of the intersection between the antenna patterns of the transmitter and bistatic receivers (range of about 1400 m for the analysed dataset) [30]. Since the aim of this work is to study the impact of

Table 2 Threshold values (simulated data)

P_{FA}	Known covariance	NSCM	FP
10^{-2}	1.13	1.23	1.25
10^{-3}	1.18	1.31	1.35
10^{-4}	1.23	1.44	1.45
10^{-5}	1.29	1.54	1.55

Palamà *et al. EURASIP Journal on Advances in Signal Processing* (2016) 2016:107

Page 10 of 17

Fig. 4 Contour plots of the P_D values as a function of the shape parameters (v_1, v_2), in the cases of known (**a**) covariance matrix, NSCM (**b**) and FP (**c**) estimates. SCR = 15 dB, CNR = 10 dB, $P_{FA} = 10^{-5}$

clutter statistics on the radar performance, the values of the bistatic and monostatic Doppler frequencies of the target were set manually, by evaluating the sea clutter spectra, in order to inject the target within the area of heavy clutter. Figure 5 shows the sea clutter spectra of the analysed data, for both horizontal and vertical polarization. The method adopted to estimate the Power Spectral Density (PSD) was the Welch periodogram [35], with a window of 512 samples and an overlap of 50 %. Each periodogram was calculated over a time interval of 15 s. We note that most spectra are centred at a normalized Doppler frequency of about 0.1. Figure 5 shows that monostatic spectrum is wider than bistatic one and VV spectra are wider than HH ones.

An important quantity to analyse is the cross-correlation between monostatic and bistatic data. The received signal model at the basis of the adopted detection scheme assumes that the signals associated with different channels are uncorrelated. Thus, the fact that two (or more) channels are actually correlated might worsen the performance of the adopted detection scheme. We separated two clutter components, i.e texture and speckle, by using the technique illustrated in [30] (by using blocks of 512 samples, resulting in a total number of blocks, N_b, equal to 250), and then, we computed the cross-correlation coefficient between the texture samples (shown in Fig. 6a) and in-phase and quadrature speckle samples (shown in Fig. 6b).

The cross-covariance function between the bistatic and monostatic textures, R_τ, was calculated as

$$R_\tau(m) = \frac{1}{N_b} \sum_{l=1}^{N_b-|m|} \left[\hat{\tau}_B(l) - \hat{\mu}_\tau^{(B)} \right] \left[\hat{\tau}_M(l+|m|) - \hat{\mu}_\tau^{(M)} \right],$$

(31)

where $\hat{\tau}_B$ and $\hat{\tau}_M$ represent the bistatic and monostatic texture, respectively, whose sample means are $\hat{\mu}_\tau^{(B)}$ and $\hat{\mu}_\tau^{(M)}$, respectively. The texture cross-correlation coefficient is $r_\tau(m) = R_\tau(m) / \left(\hat{\sigma}_\tau^{(B)} \hat{\sigma}_\tau^{(M)} \right)$, where $\hat{\sigma}_\tau^{(M)}$ and $\hat{\sigma}_\tau^{(B)}$ are the estimated standard deviations of monostatic and bistatic texture, respectively.

Concerning the analysis of the speckle, the cross-covariance function between the bistatic and monostatic in-phase speckle samples was calculated as

$$R_{s,II}(m) = \frac{1}{N_p} \sum_{l=1}^{N_p-|m|} \left[\hat{x}_{B,I}(i) - \hat{\mu}_{s,I}^{(B)} \right] \left[\hat{x}_{M,I}(i+|m|) - \hat{\mu}_{s,I}^{(M)} \right],$$

(32)

where $\hat{x}_{B,I}$ and $\hat{x}_{M,I}$ are the bistatic and monostatic in-phase speckle estimates (obtained by normalizing the clutter samples over the texture estimates), respectively, and $\hat{\mu}_{s,I}^{(B)}$ and $\hat{\mu}_{s,I}^{(M)}$ are their sample means, respectively. The cross-correlation coefficient between the in-phase components is $r_{s,II}(i) = R_{s,II}(m) / \left(\hat{\sigma}_{s,I}^{(B)} \hat{\sigma}_{s,I}^{(M)} \right)$, where $\hat{\sigma}_{s,I}^{(B)}$ and $\hat{\sigma}_{s,I}^{(M)}$ are the estimated standard deviations of the in-phase speckle components. The cross-correlation coefficient between the quadrature components, $r_{s,QQ}(m)$, is calculated similar to $r_{s,II}(m)$.

The texture cross-correlation coefficient shows a small periodicity for both HH and VV data. For VV data, there are two peaks at a time lag of about 5 and 22 s, whereas for HH data, there are peaks at about 3, 16 and 22 s. In general, VV data show higher peaks, separated by longer intervals, with respect to HH data.

The values of the speckle cross-correlation coefficient are very low for all the data, even if not null (with maximum values around 0.01), and show different behaviours, depending on polarization. For HH data, both $r_{s,QQ}$ and $r_{s,II}$ show an almost identical periodic

Table 3 NetRAD radar parameters

Radar parameters	
Carrier frequency	2.4 GHz
Transmitted signal	Up/down chirp
Bandwidth	45 MHz
Pulse duration	Variable
Pulse repetition frequency	1 kHz
Range resolution	3.33 m
Sampling frequency	100 MHz
Polarization	HH, VV (separately)
Half power beamwidth	9° (el.) × 11° (az.)

behaviour, whose fluctuations decrease with increasing time lag. For VV data, both $r_{s,QQ}$ and $r_{s,II}$ show a slightly decreasing behaviour as a function of the time lag, with the values of $r_{s,II}$ lower than the values of $r_{s,QQ}$.

In general, the analysis of the cross-correlation suggests that bistatic and monostatic data have a certain degree of correlation, which could influence the performance of the adopted detector.

4.2 False alarm regulation

In the first analysis, we studied the behaviour of the probability of false alarm as a function of the detection threshold, for the *single-channel* NAMF, applied separately on simultaneous bistatic and monostatic data. This analysis was realized also for the *multichannel* NAMF, combining the bistatic and monostatic data. In order to evaluate the robustness of the adopted detectors against the time-varying clutter spectra [36], four different values of the normalized Doppler frequency were chosen, i.e. $f_D = [-0.1, 0, 0.1, 0.2]$. As shown in Fig. 5 for the datasets collected by the NetRAD on October 21, 2010, at a bistatic angle of 30°, the clutter power is low for $f_D = -0.1$, 0 and 0.2 ($P_C < -35$ dBm) and very high for $f_D = 0.1$ ($P_C \approx -10$ dBm).

In the following, we analyse the false alarm regulation performance of the single-channel and multichannel NAMF on the HH polarized data, collected at a bistatic angle of 30°. The range cell under test is at 1400 m.

It should be noted that the total number of pulses is about 130,000 and that the number of integrated pulses (L) was set as 8. The P_{FA} was measured over bursts of L pulses, with 50 % overlap; thus, it cannot be accurately estimated for values lower than 10^{-2}.

Figure 7 shows the behaviour of the P_{FA} for the multi-channel NAMF. All the plots compare the P_{FA} values obtained at different Doppler frequencies, by employing the SCM, NSCM and FP covariance estimates. The "P_{FA}-vs-threshold" plots show that the variation of the clutter properties (in particular its non-stationarity) with the Doppler frequency influences the false alarm regulation performance. It could be noted that the maximum values of P_{FA} are obtained for a normalized Doppler frequency equal to 0.1.

From the examination of the clutter spectra, it is confirmed that the Doppler bins giving higher values of P_{FA} are included within the area where the sea clutter is more powerful and spikier. This phenomenon has been already observed and explained in [36]. For this reason, the values of P_{FA} are not constant over the entire range, and their spread is larger if the SCM estimate is used and reduced if either the NSCM or FP estimates are employed. The SCM estimate is not accurate in the case that the clutter is not Gaussian, whereas the NSCM and FP estimates are more accurate [5, 36].

By examining Fig. 7, it is possible to set suitable values of the threshold in order to achieve a desired P_{FA}. Due to the variation of P_{FA} as a function of the analysed Doppler frequency, these threshold values are not unique. A possible choice consists of adopting the average threshold, included between its maximum and minimum values. The resulting average threshold values (that were then adopted in our analysis), obtained for
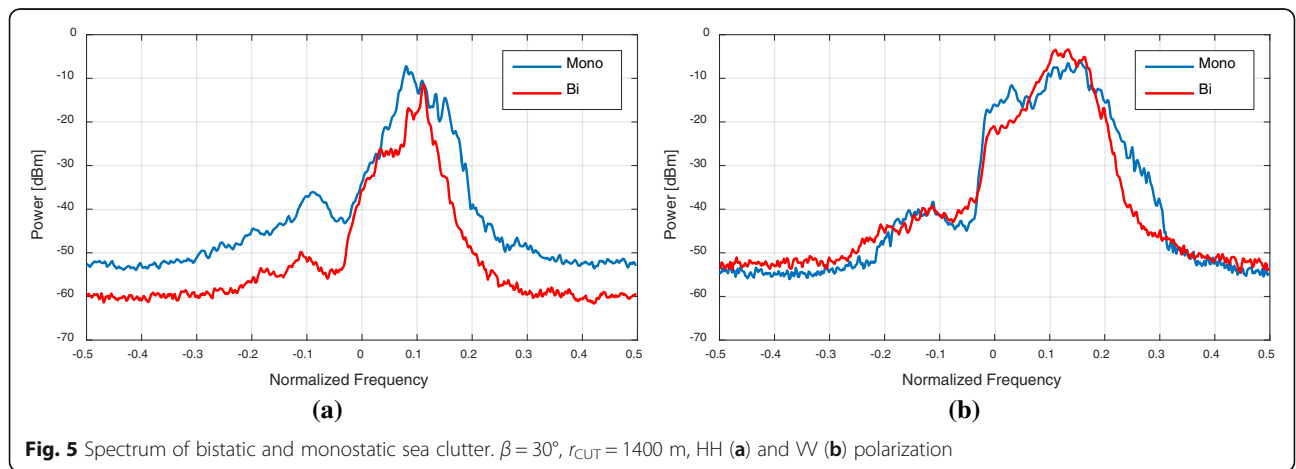

Fig. 5 Spectrum of bistatic and monostatic sea clutter. $\beta = 30°$, $r_{CUT} = 1400$ m, HH (**a**) and VV (**b**) polarization

Palamà *et al. EURASIP Journal on Advances in Signal Processing* (2016) 2016:107
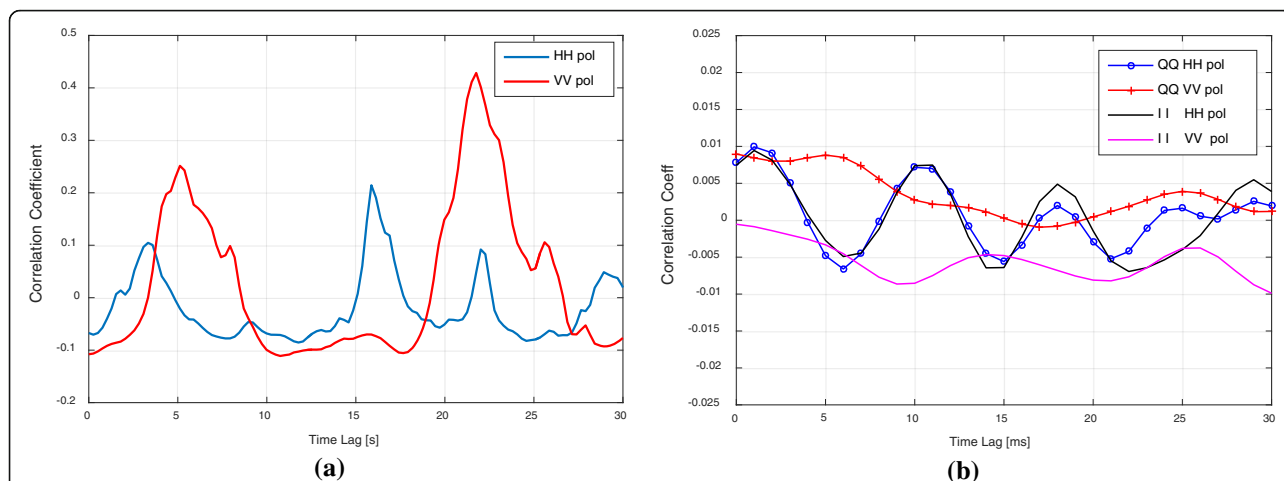
Page 12 of 17

Fig. 6 Cross-correlation between monostatic and bistatic sea clutter data, for texture (**a**) and in-phase and quadrature speckle components (**b**). $\beta = 30°$, $r_{CUT} = 1400$ m, HH and VV polarization

the analysed dataset (HH polarized data, $\beta = 30°$, $r_{CUT} = 1400$ m) and for each covariance matrix estimation method, are shown in Table 4.[2]

The false alarm regulation performance achieved by the adopted detectors (by using the chosen thresholds) is analysed as a function of the Doppler frequency, as shown in Fig. 8. In other words, for a fixed Doppler frequency, the P_{FA} values were computed for the single-channel detector, applied separately on monostatic and bistatic data and for the multichannel detector. The fluctuations of the P_{FA} values as a function of the Doppler frequency are smaller for monostatic data (Fig. 8a) with respect to bistatic ones (Fig. 8b). Both the bistatic and monostatic data show a peak of P_{FA} at $f_D \approx 0.1$, and this peak is higher for bistatic data. The overall behaviour of the P_{FA} values is matched to the clutter spectra shown in Fig. 5.

In general, the FP and NSCM estimates guarantee a more stable behaviour of the P_{FA} values, fluctuating around the desired value of 10^{-2}. The behaviour of P_{FA} seems to be less stable for the multichannel detector with respect to the single-channel one. It seems that the P_{FA} values obtained by using the multichannel detector adapt themselves to the less favourable between the bistatic and monostatic channels, i.e. the channel that, for each Doppler bin, gives P_{FA} values farther from the desired value of 10^{-2}. By comparing the covariance estimation methods, the SCM is shown to give larger fluctuations of the P_{FA} with respect to the FP and NSCM ones.

4.3 Detection performance
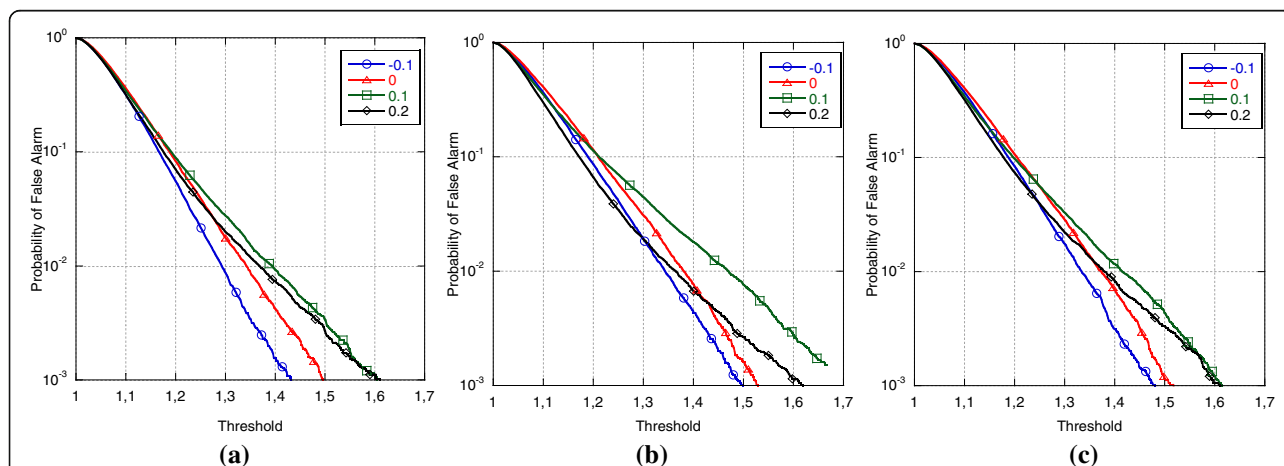In the first analysis, the detection performances of the single-channel and multichannel detectors on NetRAD

Fig. 7 P_{FA} of the *multichannel NAMF* as a function of the threshold λ, utilizing the SCM (**a**), NSCM (**b**) and FP (**c**) covariance estimate. Monostatic and bistatic data, HH polarization, $\beta = 30°$, $r_{CUT} = 1400$ m, normalized Doppler frequencies: $f_D = -0.1$ (*blue*), 0 (*red*), 0.1 (*green*), 0.2 (*black*)

Table 4 Average threshold values for PFA = 10^{-2}, evaluated on NetRAD data

	SCM	NSCM	FPE
Bi	0.79	0.84	0.83
Mono	0.81	0.85	0.83
Mono and Bi	1.35	1.42	1.38

data are examined, in terms of receiver operating characteristics, obtained for different values of the target Doppler frequency and of the signal-to-clutter ratio. The ROC curves of the multichannel NAMF are evaluated by using the SCM, NSCM and FP covariance estimates. Different values of the normalized target Doppler frequency were analysed, i.e. $f_D = [-0.1, 0, 0.1, 0.2]$, and the value of SCR was set as 0 dB. ROC curves in Fig. 9 show that the P_D values are lower for f_D equal to 0.1, where the majority of the clutter power is concentrated. On the other hand, P_D values are very high for $f_D = -0.1$. From a comparison between the covariance matrix estimators, the NSCM and FP ones give better performance than the SCM one, especially in heavy clutter conditions ($f_D = 0.1$ and, less clearly, $f_D =$ to 0 and 0.2). This is due to the fact that the SCM estimator has good performance if the statistical distribution of the disturbance samples approaches the Gaussian one, whereas the NSCM and FP estimators are accurate also in the case of non-Gaussian clutter [36].

In order to better examine the detection performance, only the heavy-clutter Doppler bin ($f_D = 0.1$) was considered. Figure 10 shows the ROC curves obtained by the single-channel and multichannel detectors for $f_D = 0.1$, for two different values of SCR (0 and 5 dB), on horizontally and vertically polarized data. By examining the single-channel NAMF detector, the P_D values are always higher for bistatic data with respect to monostatic ones,

for both HH and VV data, meaning that bistatic clutter offers, in the analysed cases, more favourable conditions for target detection. Polarization seems to have a small impact on results obtained on monostatic clutter (the P_D values are similar to HH and VV monostatic data). On the other hand, for bistatic clutter, for $P_{FA} = 10^{-2}$ and SCR = 0 dB, P_D is about 0.65 for HH and 0.5 for VV, whereas for SCR = 5 dB, P_D is about 0.82 for HH and 0.7 for VV.

In addition, the difference between the P_D values of bistatic and monostatic channels is higher for HH polarized data with respect to the VV ones. This difference could be due to the different behaviours of the shape parameter between HH and VV data, shown in [30], according to which the estimated values of the K + N shape parameters are lower in the bistatic data compared to the monostatic ones, for both polarizations (relative to the datasets collected at a bistatic angle of 30 and range cell of 1400 m).

The higher P_D values shown by the bistatic channel are consistent with the results shown in Section 3.2 for simulated data, which highlight that, for each covariance estimate, the lower the shape parameter, the higher the detection probability (this behaviour of the detection probability of the NMF detector has been shown also in [1]).

The multichannel NAMF provides a gain in performance over the single-channel NAMF. This gain is more evident for a higher value of the SCR (i.e. SCR = 5 dB). In terms of detection performance, analysed on a single Doppler bin, it is evident that, by jointly processing the signals associated with two different channels of the system, the multichannel NAMF adapts itself to the more favourable between the two channels.

The analysis of detection performance was deepened by studying the behaviour of the P_D values as a function
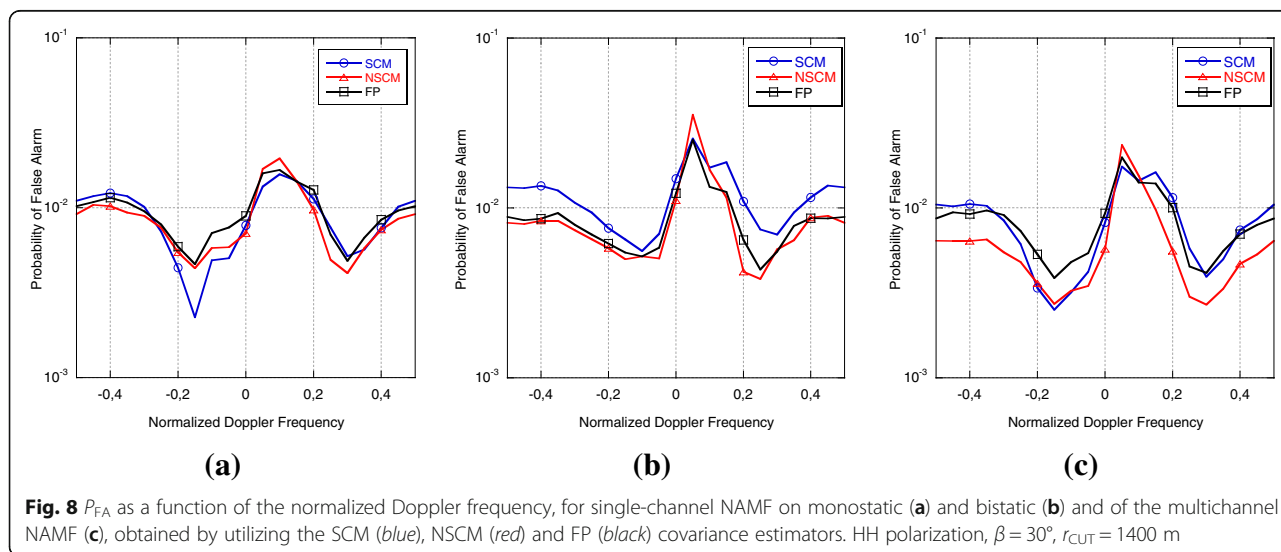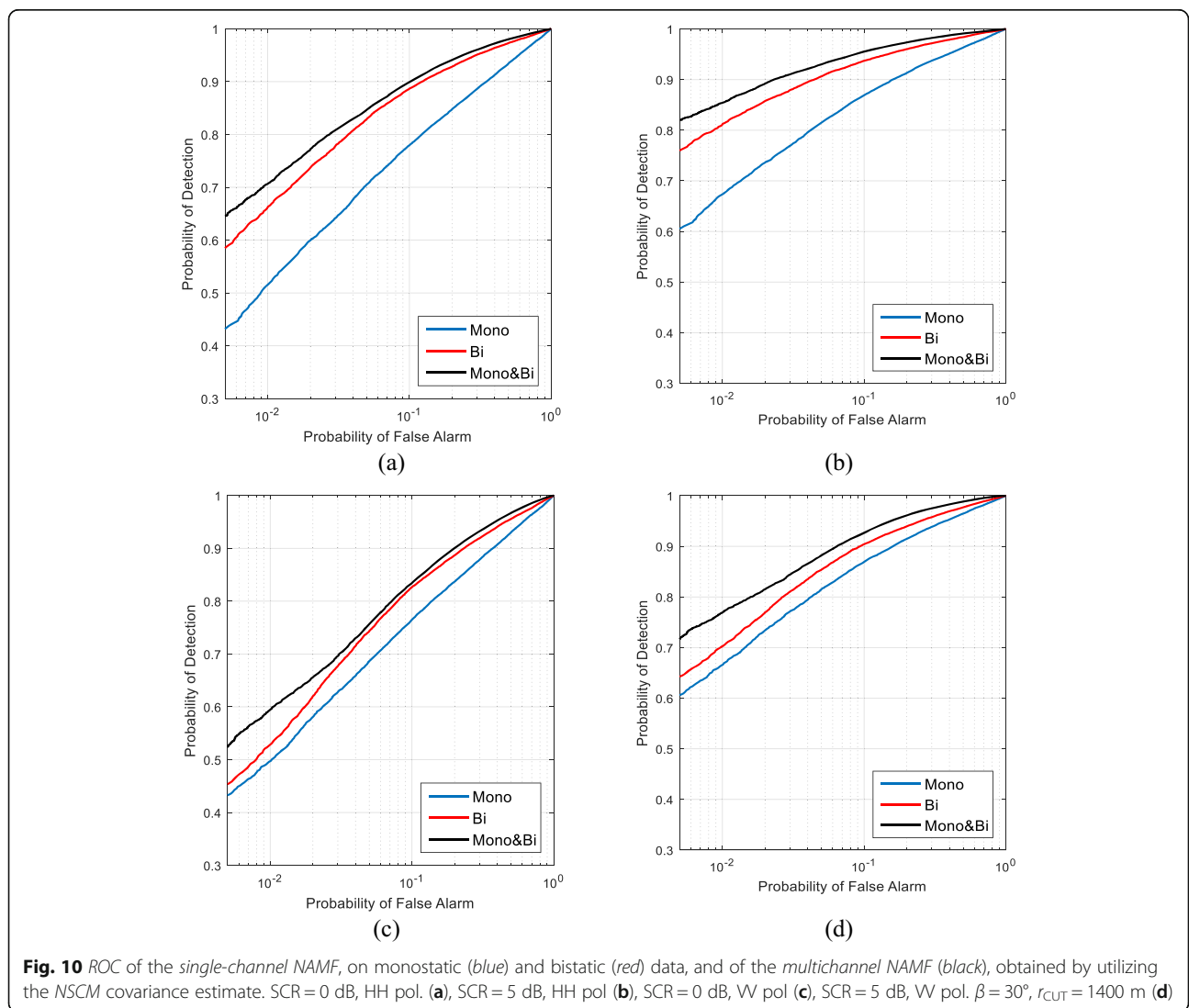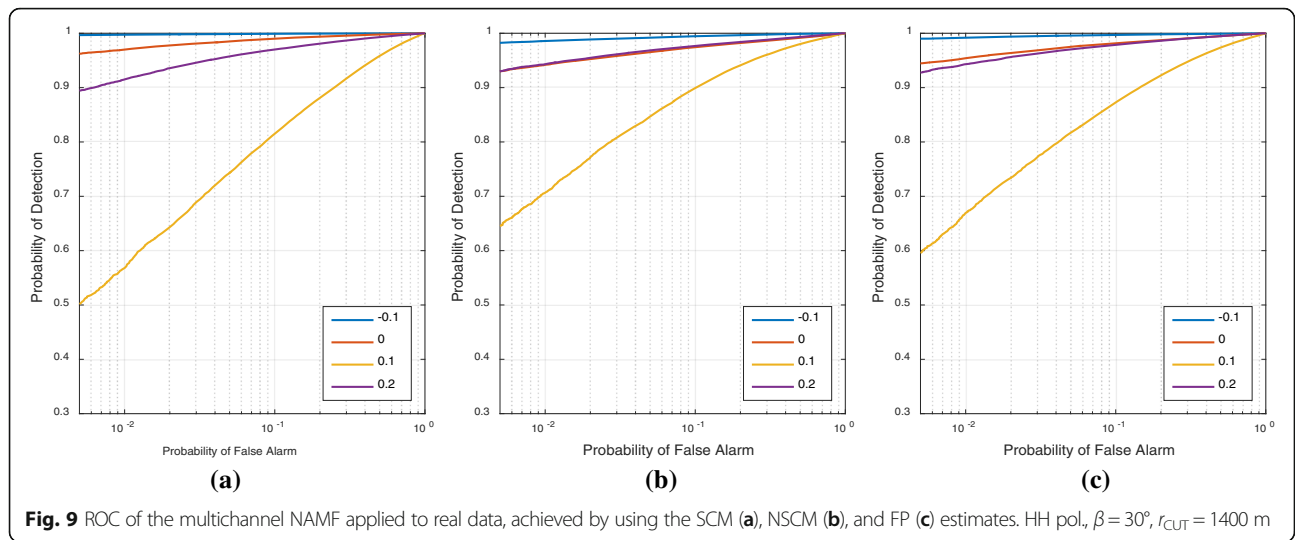

Fig. 8 P_{FA} as a function of the normalized Doppler frequency, for single-channel NAMF on monostatic (**a**) and bistatic (**b**) and of the multichannel NAMF (**c**), obtained by utilizing the SCM (*blue*), NSCM (*red*) and FP (*black*) covariance estimators. HH polarization, $\beta = 30°$, $r_{CUT} = 1400$ m

Palamà *et al. EURASIP Journal on Advances in Signal Processing* (2016) 2016:107

Page 14 of 17

Fig. 9 ROC of the multichannel NAMF applied to real data, achieved by using the SCM (**a**), NSCM (**b**), and FP (**c**) estimates. HH pol., $\beta = 30°$, $r_{CUT} = 1400$ m

Fig. 10 ROC of the *single-channel NAMF*, on monostatic (*blue*) and bistatic (*red*) data, and of the *multichannel NAMF* (*black*), obtained by utilizing the *NSCM* covariance estimate. SCR = 0 dB, HH pol. (**a**), SCR = 5 dB, HH pol (**b**), SCR = 0 dB, VV pol (**c**), SCR = 5 dB, VV pol. $\beta = 30°$, $r_{CUT} = 1400$ m (**d**)

Palamà *et al. EURASIP Journal on Advances in Signal Processing* (2016) 2016:107

Page 15 of 17

of the SCR, for a normalized Doppler of 0.1 and P_{FA} of 10^{-2}; thus, the threshold values contained in Table 4 were utilized. As the NSCM estimator seems to give better performance, it was chosen for the comparison between single-channel and multichannel detectors.

Synthetic clutter samples were also generated, with similar statistical properties as the analysed real data. Clutter samples were generated according to the K-plus-noise distribution, whose parameters were estimated from real data through the Method of Moments [30]. For the HH data, shape parameter ν is 0.047 for bistatic data and 0.057 for monostatic data, whereas for VV data, ν = 0.064 for bistatic and ν = 0.091 for monostatic data.

The clutter autocorrelation was also estimated for each analysed dataset, where the symbol (.)* indicates the complex conjugate. The clutter samples were generated with the extracted correlation properties.

Figure 11 shows the "P_D-vs-SCR" curves of the single-channel NAMF and of the multichannel NAMF, applied to real and simulated data.

For the real data, Fig. 11a shows that, for a P_D of 0.8, the multichannel NAMF gives a SCR gain of about 1.5 and 6 dB over the single-channel NAMF applied on bistatic and monostatic data, respectively. The corresponding values for VV data (Fig. 11b) are 1 and 4 dB.

The behaviour of P_D is more flat for simulated data with respect to real ones, which means that the SCR has a higher impact when real clutter is processed. Relative to the single-channel detector, the gap between bistatic and monostatic data is similar to real and simulated data. On the other hand, we note a large deviation in the detection performance of the multichannel detector, between real and simulated data. In the case

of real data, the P_D values achieved by the multichannel detector are not far from the ones obtained by using the single-channel detector on bistatic data. In the simulated data, a large gap is noticeable between the multichannel and the single-channel curves. In other words, the gain achieved by using a multichannel detection scheme is larger for simulated data with respect to real ones. One of the factors that could influence this different behaviour is that real bistatic and monostatic data show (Fig. 6) to be correlated, whereas simulated data are generated independently (i.e. they are uncorrelated). As the detection scheme is derived by assuming that the channels are uncorrelated, its performance is expected to be generally higher if this assumption is verified.

5 Conclusions

This work concerns suboptimum radar detection technique that combines the signal received by the nodes of a multistatic radar, in the case of non-Gaussian disturbance. The adopted multichannel detection scheme, called multichannel normalized adaptive matched filter, is able to keep constant the probability of false alarm, for different clutter conditions associated with the nodes of the system.

A derivation of the multichannel NAMF has been illustrated, as an alternative to the one already provided by authors in [23]. The performance of the multichannel NAMF has been evaluated, showing that clutter statistical diversity influences the detection performance. We have studied the behaviour of the P_D values as a function of the couple of shape parameters, associated with the two channels of the simulated system. The results have shown that, in the case of two channels, the contour
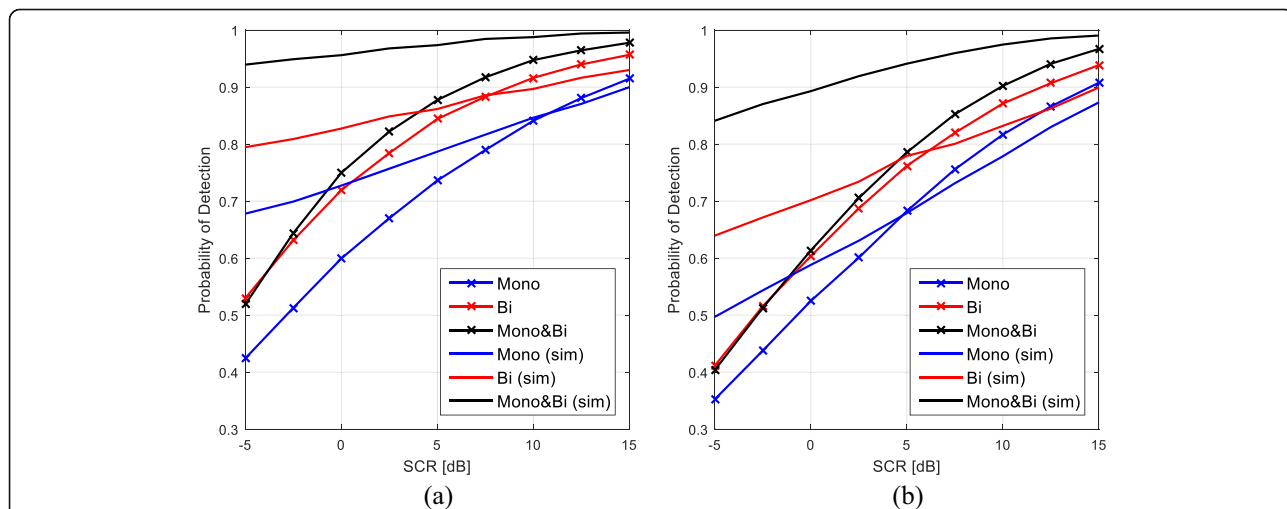

Fig. 11 P_D as a function of *SCR* of the *single-channel NAMF*, on monostatic (*blue marked*) and bistatic (*red marked*) data, and of the *multichannel NAMF* (*black marked*), obtained by utilizing the *NSCM* covariance estimate, compared with P_D values obtained on simulated data fixed $P_{FA} = 10^{-2}$. HH (**a**) and VV (**b**) polarization, β = 30°, r_{CUT} = 1400 m

plots of P_D as a function of the clutter shape parameters are similar to hyperbolas, meaning that the same value of P_D can be obtained for different couples of shape parameters. The performance analysis has been carried out also on real sea clutter data, combining the bistatic and monostatic clutter data collected by the nodes of the NetRAD system. The false alarm regulation performance of the multichannel NAMF seem to be slightly lower than the one of the single-channel NAMF, applied separately on bistatic and monostatic data. In particular, the behaviour of the P_{FA} values of the multichannel NAMF, for each Doppler bin, seems to adapt to the less favourable between the two system nodes. This behaviour is not desirable; thus, it should be better studied in future research steps.

The detection performance evaluation has shown that the multichannel NAMF gives a gain over the single-channel one, which is larger in the horizontally polarized data than in vertically polarized ones. If the multichannel detector is employed, the P_D values are higher in the case of simulated data with respect to real ones. A possible reason is that, in real data, the channels are not uncorrelated, whereas the multichannel NAMF has been derived from the assumption of independent channels. In future research steps, this assumption will be possibly removed, in order to derive a detection scheme that exploits the whole information carried on by the radar channels, by processing them jointly and not separately. In [37], the authors remove the aforementioned assumption and derive a detection scheme in the case of Gaussian clutter. It would be of interest to consider the case where the clutter samples are compound Gaussian distributed and correlated across channels.

6 Endnotes
[1]It should be noted that another possible representation adopts $MN \times MN$-sized blocks, whose total number is L^2.

[2]The P_{FA} versus threshold plots for the single-channel detector, applied separately to monostatic and bistatic data, are not shown for lack of space.

References
1. E Conte, M Lops, G Ricci, Asymptotically optimum radar detection in compound-Gaussian clutter. IEEE Trans. Aerosp. Electron. Syst. **31**(2), 617–625 (1995)
2. F Gini, Sub-optimum coherent radar detection in a mixture of K-distributed and Gaussian clutter. IEE Proc. Radar Sonar Navig. **144**(1), 39–48 (1997)
3. S Kraut, LL Scharf, The CFAR adaptive subspace detector is a scale-invariant GLRT. IEEE Trans. Signal Process. **47**(9), 2538–2541 (1999)
4. E Conte, A De Maio, G Ricci, Recursive estimation of the covariance matrix of a compound-Gaussian process and its application to adaptive CFAR detection. IEEE Trans. Signal Process. **50**(8), 1908–1915 (2002)
5. F Gini, M Greco, Covariance matrix estimation for CFAR detection in correlated heavy tailed clutter. Signal Process. **82**(12), 1847–1859 (2002)
6. F Pascal, Y Chitour, JP Ovarlez, P Forster, P Larzabal, Covariance structure maximum-likelihood estimates in compound Gaussian noise: existence and algorithm analysis. IEEE Trans. Signal Process. **56**(1), 34–48 (2008)
7. E Conte, E D'Addio, A Farina, M Longo, Multistatic radar detection: synthesis and comparison of optimum and suboptimum receivers. IEE Proc. Commun. Radar Signal Process. **130**(6), 484–494 (1983)
8. E D'Addio, A Farina, Overview of detection theory in multistatic radar. IEE Proc. F Commun. Radar Signal Process. **133**(7), 613–623 (1986)
9. V Chernyak, *Fundamentals of multisite radar systems* (Amsterdam, 1995)
10. E Fishler, A Haimovich, RS Blum, LJ Cimini, D Chizhik, RA Valenzuela, Spatial diversity in radars—models and detection performance. IEEE Trans. Signal Process. **54**(3), 823–838 (2006)
11. J Li, P Stoica, *MIMO radar signal processing* (Wiley, Hoboken, 2009)
12. A De Maio, M Lops, Design principles of MIMO radar detectors. IEEE Trans. Aerosp. Electron. Syst. **43**(3), 886–898 (2007)
13. AM Haimovich, RS Blum, LJ Cimini, MIMO radar with widely separated antennas. IEEE Signal Process. Mag. **25**(1), 116–129 (2008)
14. M Barkat, PK Varshney, Decentralized CFAR signal detection. IEEE Trans. Aerosp. Electron. Syst. **25**(2), 141–149 (1989)
15. RS Blum, SA Kassam, HV Poor, Distributed detection with multiple sensors: part II—advanced topics. Proc. IEEE **85**(1), 64–79 (1997)
16. F Gini, F Lombardini, L Verrazzani, Robust monoparametric multi-radar CFAR detection against non-Gaussian spiky clutter. IEE Proc. Radar Sonar Navig. **144**(3), 131–140 (1997)
17. F Gini, F Lombardini, PK Varshney, On distributed signal detection with multiple local free parameters. IEEE Trans. Aerosp. Electron. Syst. **35**(4), 1457–1466 (1999)
18. F Gini, F Lombardini, L Verrazzani, Decentralised detection strategies under communication constraints. IEE Proc. Radar Sonar Navig. **145**(3), 199–208 (1998)
19. JH Michels, P Varshney, D Weiner, Multichannel signal detection involving temporal and cross-channel correlation. IEEE Trans. Aerosp. Electron. Syst. **31**(3), 866–880 (1995)
20. NA Goodman, D Bruyere, Optimum and decentralized detection for multistatic airborne radar. IEEE Trans. Aerosp. Electron. Syst. **43**(2), 806–813 (2007)
21. P Wang, H Li, B Himed, Moving target detection using distributed MIMO radar in clutter with nonhomogeneous power. IEEE Trans. Signal Process. **59**(10), 4809–4820 (2011)
22. G Cui, L Kong, X Yang, Multiple-input multiple-output radar detectors design in non-Gaussian clutter. IET Radar Sonar Navig. **4**(5), 724–732 (2010)
23. CY Chong, F Pascal, J-P Ovarlez, M Lesturgie, MIMO radar detection in non-Gaussian and heterogeneous clutter. IEEE J. Sel. Top. Signal Process. **4**(1), 115–126 (2010)
24. WA Al-Ashwal, K Woodbridge, HD Griffiths, Analysis of bistatic sea clutter part I: average reflectivity. IEEE Trans. Aerosp. Electron. Syst. **50**(2), 1283–1292 (2014)
25. WA Al-Ashwal, K Woodbridge, HD Griffiths, Analysis of bistatic sea clutter part II: amplitude statistics. IEEE Trans. Aerosp. Electron. Syst. **50**(2), 1293–1303 (2014)
26. E Conte, M Longo, Characterization of radar clutter as a spherically invariant random process. IEE Proc. **134**(2), 191–197 (1987)
27. K Ward, R Tough, S Watts, *Sea clutter: scattering, the K distribution and radar performance* (IET, London, 2013)
28. A Farina, F Gini, MV Greco, L Verrazzani, High resolution sea clutter data: statistical analysis of recorded live data. IEE Proc. Radar Sonar Navig. **144**(3), 121 (1997)
29. R. Palamà, M. Greco, P Stinco, F Gini, "Statistical analysis of netrad high resolution sea clutter", *21st European Signal Processing Conference (EUSIPCO 2013)*, Marrakech, 2013, pp. 1-5.
30. R Palamà, MS Greco, P Stinco, F Gini, "Statistical analysis of bistatic and monostatic sea clutter", *IEEE Transactions on Aerospace and Electronic Systems*, vol. 51, no. 4, pp. 3036-3054, Oct. 2015.
31. E Ollila, DE Tyler, Distribution-free detection under complex elliptically symmetric clutter distribution, in *Proc. IEEE 7th Sensor Array Multichannel Signal Processing Workshop (SAM), Hoboken, NJ*, 2012, pp. 413–416

Palamà *et al. EURASIP Journal on Advances in Signal Processing* (2016) 2016:107

Page 17 of 17

32. F Gini, JH Michels, Performance analysis of two covariance matrix estimators in compound-Gaussian clutter. IEE Proc. Radar Sonar Navig. **146**(3), 133–140 (1999)

33. F Gini, M Greco, Suboptimum approach to adaptive coherent radar detection in compound-Gaussian clutter. IEEE Trans. Aerosp. Electron. Syst. **35**(3), 1095–1104 (1999)

34. E Ollila, DE Tyler, V Koivunen, HV Poor, Complex elliptically symmetric distributions: survey, new results and applications. IEEE Trans. Signal Process. **60**(11), 5597–5625 (2012)

35. P Stoica, R Moses, *Spectral analysis of signals* (Prentice Hall, Upper Saddle River, 2005)

36. M Greco, P Stinco, F Gini, M Rangaswamy, Impact of sea clutter nonstationarity on disturbance covariance matrix estimation and CFAR detector performance. IEEE Trans. Aerosp. Electron. Syst. **46**(3), 1502–1513 (2010)

37. CY Chong, F Pascal, J Ovarlez, M Lesturgie, Robust MIMO radar detection for correlated subarrays, in *IEEE International Conference on Acoustics, Speech and Signal Processing (ICASSP)*, 2010, pp. 2786–2789

38. E Conte, A De Maio, E Conte, A De Maio, Mitigation Techniques for Non-Gaussian Sea Clutter. IEEE Journal of Oceanic Engineering **29**(2):284–302 (2004)

39. KJ Sangston, F Gini, MV Greco, A Farina, KJ Sangston, F Gini, MV Greco, A Farina, Structures for radar detection in compound Gaussian clutter. IEEE Transactions on Aerospace and Electronic Systems **35**(2):445–458.

40. F. Gini, M.V. Greco, A. Farina, P. Lombardo, F. Gini, M.V. Greco, A. Farina, P. Lombardo, Optimum and mismatched detection against K-distributed plus Gaussian clutter. IEEE Transactions on Aerospace and Electronic Systems **34**(3):860–876.